Journal of Fluids and Structures 26 (2010) 559–578

JOURNAL OF
FLUIDS AND
STRUCTURES

www.elsevier.com/locate/jfs

Thickness effect of NACA foils on hydrodynamic global parameters, boundary layer states and stall establishment

C. Sarraf[a], H. Djeridi[b,*], S. Prothin[a], J.Y. Billard[a]

[a]*Institut de Recherche de l'Ecole Navale (IRENav, EA 3634), Ecole Navale BP 600, Lanvéoc Poulmic, 29240 Brest Armées, France*
[b]*Université Européenne de Bretagne, Université de Brest, Laboratoire de Physique des Océans, UMR 6523, 6 Avenue Le Gorgeu, BP 809, 29285 Brest Cedex, France*

Received 2 October 2008; accepted 17 February 2010
Available online 24 April 2010

Abstract

The present study experimentally investigates the hydrodynamic behaviour of 2-D NACA (15%, 25% and 35%) symmetric hydrofoils at Reynolds number 0.5×10^6. Particular attention was paid to the hysteretic behaviour at the static stall angle, and a detailed cartography of the boundary layer structures (*integral quantities and velocity profiles*) is given to support the detachment mechanism and the onset of von Kármán instability for thick hydrofoils.

Keywords: Lift and drag; Thick foils; Boundary layer; Von Kármán street

---

1. Introduction

Flow past bluff bodies at high incidence angles or past a cylinder has been the object of a considerable number of studies, and they have shed light on the different flow regimes according to the Reynolds number, boundary layer conditions, free-stream turbulence intensity, aspect ratio and thickness effects. The main feature of this class of flow is the establishment of the von Kármán vortices persisting at high Reynolds numbers in the turbulent regime. Many studies have been devoted to vortices resulting from a global instability, longitudinal vortices (secondary instability), small-scaled Kelvin–Helmholtz vortices (convective instability in the shear layer) and the nonlinear interactions between the organised and chaotic part of the flow motion for this class of flow [e.g., Williamson, 1992; Persillon and Braza, 1998; Cantwell and Coles, 1983; Perrin et al., 2005; Braza et al., 2006; Perrin et al., 2008]. These previous studies have provided databases for numerical turbulence modelling in which the nonlinear interactions between the organised and chaotic characteristics of the flow must be taken into account. Nevertheless, vortex shedding was well established for this class of flows, and few studies have been devoted to the hysteretic behaviour of the development of the Kármán street. This behaviour is linked to the static stall of the lifting-body configuration at high incidence angles, where the hysteretic loop is associated with two kinds of flows (partially attached and massively detached) in the context of non-antisymmetric vortex shedding [the shed vortex close to the trailing edge is weakened by the opposite vortex close to the leading edge which starts being shed (Hoarau et al., 2003)]. With regard to lifting bodies, numerous works have focused on flat plate boundary layers with and without adverse pressure gradients (Na and Moin, 1998; Yang and Voke, 2001;

---

[*] Corresponding author. Tel.: +33 2 98 01 83 12; fax: +33 2 98 01 64 68.
E-mail address: henda.djeridi@univ-brest.fr (H. Djeridi).

0889-9746/$ - see front matter © 2010 Elsevier Ltd. All rights reserved.
doi:10.1016/j.jfluidstructs.2010.02.004

Nomenclature

$C_f = 0.246\mathrm{Re}_{\delta_2^{-0.268}}/10^{0.678H_{12}}$ friction coefficient (Ludwieg–Tillman)
$C_p = 1-(U_e/U_{ref})^2$ pressure coefficient
$H_{12} = \delta_1/\delta_2$ shape factor
U_e external velocity
$u = U_e\sqrt{C_f/2} = \sqrt{\tau_w/\rho}$ shear stress velocity
$u^+ = A\log y^+ + B$ tangential velocity using inner coordinates
$u^+ = f(y^+) + \frac{\Pi}{\kappa}\omega(y/\delta)$ Coles law for $y+ > 100$
$y^+ = yu_*/v$ inner variable for normal position
δ boundary layer thickness
$\delta_1 = \int_0^\delta (1-u)/(U_e)\,dy$ displacement thickness
$\delta_2 = \int_0^\delta (1-u)/(U_e)\frac{u}{U_e}\,dy$ momentum thickness
$\tau = \rho u^2 + \frac{\partial p}{\partial x}y$ wall shear stress using adverse pressure gradient
$\tau_w = \mu\frac{\partial U}{\partial y}\big|_{y=0}$ wall shear stress

Perry and Marušic, 1995; Marušic and Perry, 1995), but few recent papers deal with boundary layers on hydrofoils and vortex shedding (Bourgoyne et al., 2003, 2005). An increasing interest in boundary layers at high incidence angles, can be noticed to predict the types of hysteretic loops that may occur (Mittal and Saxena, 2000; Sicot et al., 2006) and to quantify the unsteady oscillatory flow in the near-wake that produces pressure fluctuations, which are sources of hydroacoustic noise (Bourgoyne et al., 2000). In addition, experiments have been performed to explore the unsteady separating of boundary layers (Lurie et al., 1998), and the influence of laminar separation and transition on hysteresis on particular lifting bodies (Mueller, 1985); however, in these few references, no systematic study of the effect of hydrofoil thickness and vortex dynamics on the onset of the organised modes of the vortex shedding during a hysteretic loop has been undertaken. One of the main interests of thick hydrofoils is the stall delay that such profiles can provide when used at a high incidence angle. In spite of the increasing number of applications, thick foil behaviour is not clearly understood. Very little data are available to describe the turbulent boundary layer structures, performance control, unsteady separated flows, vibrations and hydrodynamic behaviour at low and high angles of incidence. The effect of the hydrofoil thickness, which leads to an increase in the lift coefficient, has been studied by Thwaites (1960) and can be observed on hydrofoils with relative thicknesses (t/c, where t is the maximum thickness of the foil and c its chord length) greater than 10%. Although some studies have been devoted to thickness effects on global parameters, few of them have investigated the details of the flow in the boundary layer with adverse pressure gradients (Bourgoyne et al., 2000). The present work intends to clarify this point.

The present work proposes such a study and investigates flows on three NACA symmetric foils (15%, 25% and 35% relative thickness) at a Reynolds number of 0.5×10^6 based on chord length. One of the objectives is to provide a refined database with respect to the near wall fields; allowing access to the key physical properties related to the detachment of the turbulent boundary layer on thick bodies. A deliberate choice was made to perform field measurements in the near-wall and near-wake region with spatial and temporal refinement, using non-intrusive laser doppler velocimetry (LDV) and particle image velocimetry (PIV) techniques. This choice constitutes a first essential step to allow a thorough quantification of the laminar to turbulent transition, the detachment of the turbulent boundary layer subjected to the adverse pressure gradient and the establishment of the von Kármán instability. The objectives of the present study are summarised as follows:

(i) to provide a detailed evaluation of the mean and turbulent quantities of the boundary layer in the profiles near the separation region with a strong adverse pressure gradient;
(ii) to quantify the scaling laws of the boundary layer and provide a detailed cartography of the mean velocity components during static stall; and
(iii) to analyse the unsteady behaviour due to the coherent structures' formation at high incidence by means of spectral analysis and vortex core detection during the hysteretic stall process;

The paper is organised as follows. Section 2 presents the experimental set-up, flow configurations and measurements. Section 3 is devoted to the results concerning the thickness effects and global parameters. Section 4 presents the topology of the unsteady, separated flow during the hysteretic behaviour of the detachment and the formation of the vortex.

2. Experimental set-up and measurements

The experiments were conducted in the hydrodynamic tunnel of the French Naval Academy, Fig. 1(a). This facility contains a test section that is 1 m long and has a square cross section measuring $0.192\times0.192\,\mathrm{m}^2$ in which a maximum

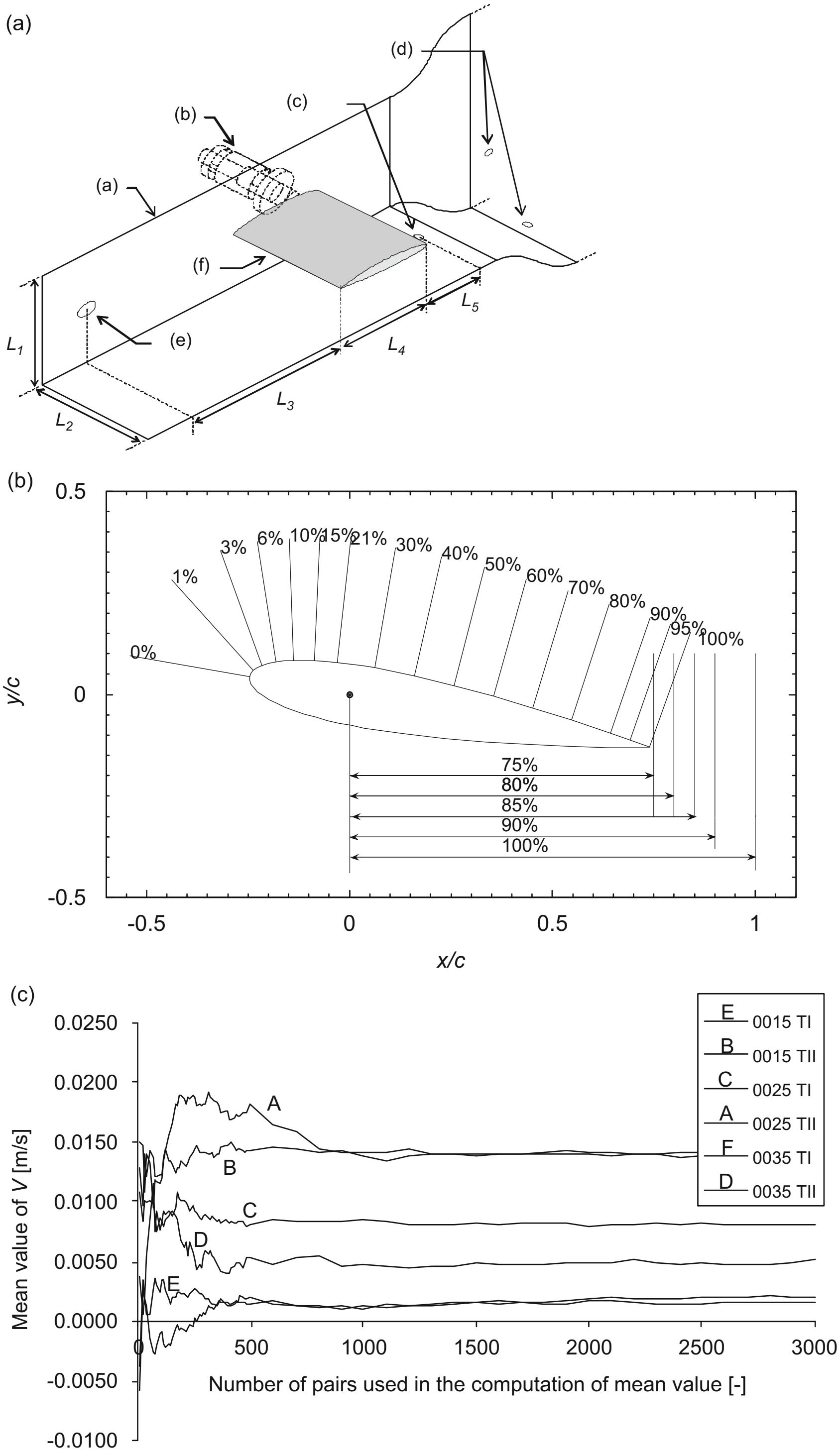

Fig. 1. **(a)** Experimental set-up: (a) back wall of the vein, (b) force balance, (c) downstream pressure tap, (d) upstream pressure tap, (e) acoustical pressure sensor, (f) profile, $L_1 = L_2 = 192\,\text{mm}$, $L_3 = 625\,\text{mm}$, $L_4 = 100\,\text{mm}$, $L_5 = 225\,\text{mm}$. **(b)** LDV measurement locations. **(c)** Statistical convergence test for the PIV measurements: mean vertical component of velocity versus number of pairs of images.

velocity of 15 m/s can be achieved. The turbulence intensity upstream of the entrance of the test section is 2%. The three designed hydrofoils are two-dimensional symmetric profiles with relative maximum thicknesses of 15%, 25% and 35% located 25% from the leading edge. The experiments were performed with a cord length of 100 mm and a span length of 192 mm at a Reynolds number based on the chord length of 0.5×10^6, which corresponds to an upstream velocity of 5 m/s. The blockage ratios defined as t/H (H being the height of the test-section) were 0.078 for the NACA0015 and 0.182 for the NACA0035. The experimental facilities are detailed in Djeridi et al. (2007). The lift and drag measurements were performed using a resistive gauge hydrodynamic balance calibrated in our laboratory. The mean and root mean square (*rms*) values were calculated from 30-s test measurements carried out at 1830 Hz. The determination of the hydrodynamic parameters was performed for incidence angles α in the range [0°, 40°], and the maximum range of the balance was 0–180daN for the lift force and 0–17daN for the drag force.

To characterise the structure of the boundary layer and the near wake that develop on the hydrofoil, detailed velocity measurements were performed by LDV techniques, using a refined spatial grid. Two components, three beams LDV Dantec Dynamics™ system was used to measure the normal and tangential velocities in water seeded with micron-size, silver-plated, glass spheres. The system was operated in backward scattering mode and was coupled with two enhanced burst spectrum analysers. Excellent visibility of the signal was achieved with a very low signal-to-noise ratio. The time histories were recorded with 8000–20 000 samples acquired in a range of 20–60 s. In the sublayer, the number of collected samples fell to about 8000. These parameters correspond to mean data rates of 1000–130 Hz and are sufficient to obtain the mean velocities and rms values with an uncertainty estimated by statistical considerations to be less than 1% and 1.5%, respectively. These uncertainties were determined from statistical methods related to the normal law that were applied to a distribution of 20000 samples. A remote mechanical positioning system with a minimum translation step of 10 μm allowed us to measure the velocity field around the hydrofoil along a curvilinear map (x, y). The plan of measurements is located at a quarter of the spanwise length L. The dimensions of the probe volume are 0.4 mm in the spanwise direction and 0.05 mm in both vertical and longitudinal directions. Velocity measurements were performed in the boundary layer from the leading to the trailing edge ($0<x/c<1$) on 16 normal lines (~70 measurements per normal line). At each location, measurements were performed normal to the wall from the outer region of the boundary layer to the wall, Fig. 1(b). The closest measurements resulted in a mean distance to the wall of 50 μm; corresponding to $y^+ = 3$–8 in the turbulent boundary layer. In the chordwise direction, measurements were taken every $x/c = 0.1$ for every $y/c = 5\times10^{-4}$. To determine the laminar to turbulent transition with an accuracy of $0.02x/c$, the grid was locally refined in the chordwise direction.

Concerning unsteady, separated states, a spectral analysis was conducted in the shear layer downstream and in the wake of the foils using a maximum data rate of 2000 Hz for 400 s samples; leading to a spectral resolution of 0.25 Hz. Spectral analysis of the vertical velocity components was obtained by applying the fast Fourier transform method to the re-sampled signals.

The PIV measurements were carried out with the same Reynolds number for the three hydrofoils at high incidence during the static stall. A double pulse ND:YAG Quantel laser was used, and delivers 2 × 20 mJ/pulse that illuminates the polyamide seed particles with a 1-mm thick light sheet. The size of the particles was about 10 μm. A PCO-sensicam camera with a resolution of 1280 × 1024 pixels was used and recorded double, full-frame particle images. The camera was equipped with a 60-mm objective lens with a diaphragm aperture of 1.2. The camera and laser system was operated at a frequency of 4 Hz.

The size of the measurement area was $-0.468<x/c<0.508$ and $-0.268<y/c<0.533$. The flow was analysed by cross-correlating 50% overlapping windows of 32 × 32 pixels. This yield of 79 × 63 vectors and 3000 pairs of images was analysed to generate the converged flow field statistics. The statistical convergence was tested using an increasing number of pairs of images, and convergence was reached beyond 2000 pairs of images for the mean velocity and rms values. This test is shown in Fig. 1(c) for the case of the vertical component of velocity, which is the slowest to converge. All of the results presented were determined using 3000 pairs of images.

3. Thickness effects on global parameters

3.1. Lift and drag measurements

Classical behaviour of both the lift and drag coefficients is observed in Fig. 2 for low incidence angles. An abrupt loss of lift, which is characteristic of stall, is observed on the NACA0015 and the NACA0025 for higher angles. The lift behaviour of the two thinner profiles was linear for small incidence angles. For the thicker profile, a screen effect delays the establishment of the lift; leading to nonlinear behaviour for small angles of attack. It can be noticed that the linear range of incidence angles increases with the thickness of the profile. The angles limiting the linear behaviour are 7°, 13° and 16° and stall appears for angles of 21°, 33° and 40° for the hydrofoils with 15%, 25% and 35% relative thickness, respectively.

The evolution of the drag coefficient follows classical trends for low incidence the effect of thickness is visible by an augmentation of the drag coefficient as thickness increases. On these curves, the onset of stall is linked to a violent

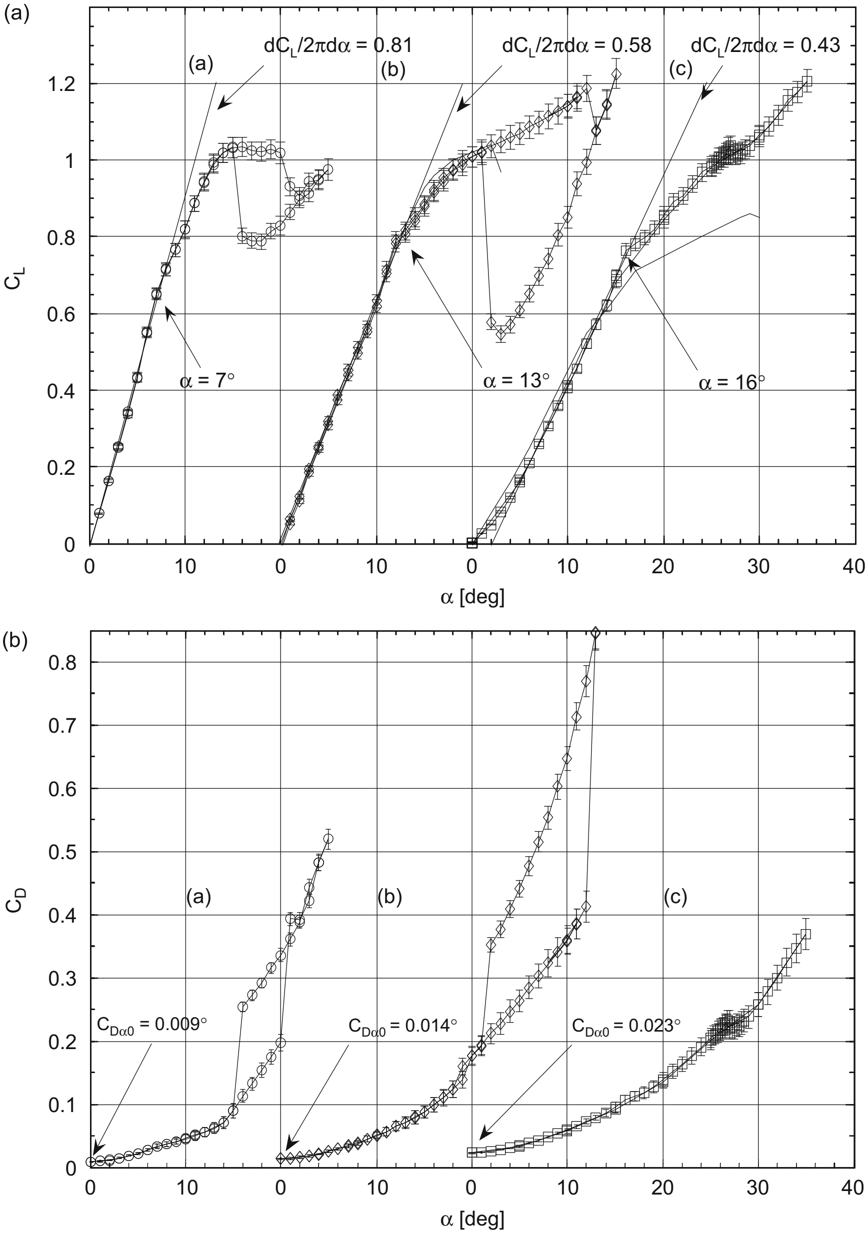

Fig. 2. Hydrodynamic coefficients for the three NACA profiles (a) NACA0015, (b) NACA0025 and (c) NACA0035 versus incidence angle. Top: lift coefficients, C_L; bottom: drag coefficients, C_D.

increase in the drag coefficient; however, this is not observed for the NACA0035 because stall appears at incidences beyond the range of the gauge balance. The thickness effect introduces a decrease in the slope of the lift coefficient as thickness increases, which is characteristic of thick profiles. Hysteretic behaviour will be discussed in the large incidence angle section.

3.2. Turbulent boundary layer states

For each measurement point, 20 000 samples were validated during a maximum interval of 60 s (corresponding to the near wall locations). This was proven sufficient after performing tests to measure the mean and the rms values of the *u* and

v velocity components to ensure convergence and repeatability. According to the previously refined grid, a survey of the distribution of the mean tangential and normal velocity components is presented. First, our goal was to characterise the boundary shape parameters on the NACA0015, NACA0025 and NACA0035 hydrofoils. The velocity profiles were numerically integrated to compute the displacement, δ_1, momentum, δ_2, and the thicknesses from which the shape factor, H_{12}, is deduced. In our case, the external velocity was the maximum velocity measured on the normal line.

The shape factor is presented in Fig. 3(a) against the normalised chord length. It can be observed that the thickness effect is associated with an increase in the length of the laminar region near the leading edge, which grows from less than 10% on the NACA0015 to 30% on the NACA0035. After the transition, the value of H_{12} remains equal to 1.6 (larger than the value observed for the turbulent boundary layer, which was 1.4). It must be noted that this value rigorously depends on the Reynolds number (Cousteix, 1989) and the pressure gradient. Near the trailing edge, the shape factor was less than three on the two thinner profiles and greater than four on the third, on which separation was observed. These values are consistent with the threshold values proposed by Bradshaw (1967).

To check self-similarity and to quantify the thickness effect of the foils on the boundary layer, the mean velocity profiles with inner variables are presented. Inner variables are classically defined as y^+ for the normal position and u^+ for the tangential component of the velocity. To determine the value of the shear stress velocity, u^*, an efficient estimation of the skin friction was required. The friction was determined using an experimental model based on the value of the integral quantities proposed by Ludwieg and Tillman (1950) and compared with the direct evaluation of the near wall velocity gradient, Fig. 3(b). A complete analysis of the method and the uncertainty of the near wall velocity gradient measurement can be found in Sarraf (2007).

Fig. 4 shows the velocity profiles for the three foils at different locations on x/c using a scaling law. It can be seen that the slopes of the profiles in the logarithmic region are quite far from the classical value of 5.75 obtained for turbulent boundary layers on flat plates. This effect is due to the adverse pressure gradient and has been quantified by Mellor and Gibson (1966) and Mellor (1966).

Moving downstream, the velocity profiles were characterised by the shape of the wake region. For the x/c locations near the trailing edge, the wake area can be described by a second law proposed by Coles (1956) for $y^+ > 100$. The hypothesis of a universal wake function is reported in Fig. 4 for the three profiles at the different x/c locations. The thickness effect is then characterised by a deviation of the wake law, this deviation is steeper for the two thicker hydrofoils.

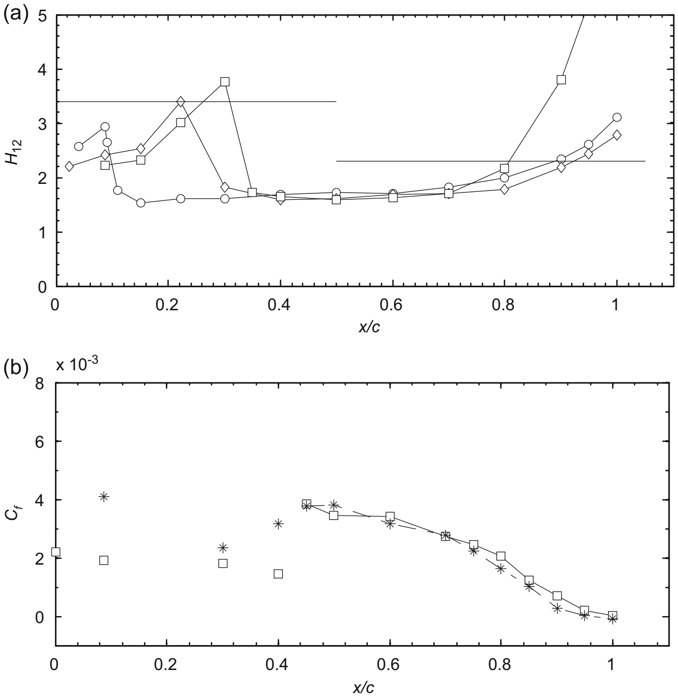

Fig. 3. (a) Shape factors for the three NACA profiles, Re = 5×10^5, $\alpha = 10°$: ○, NACA0015, ◇, NACA0025, □, NACA0035. (b) Skin friction evolution versus x/c. □, C_f obtained from the Ludwieg–Tillman formula; *, C_f estimated using velocity gradient. Example for NACA0035 at Re = 0.5×10^6 and $\alpha = 5°$.

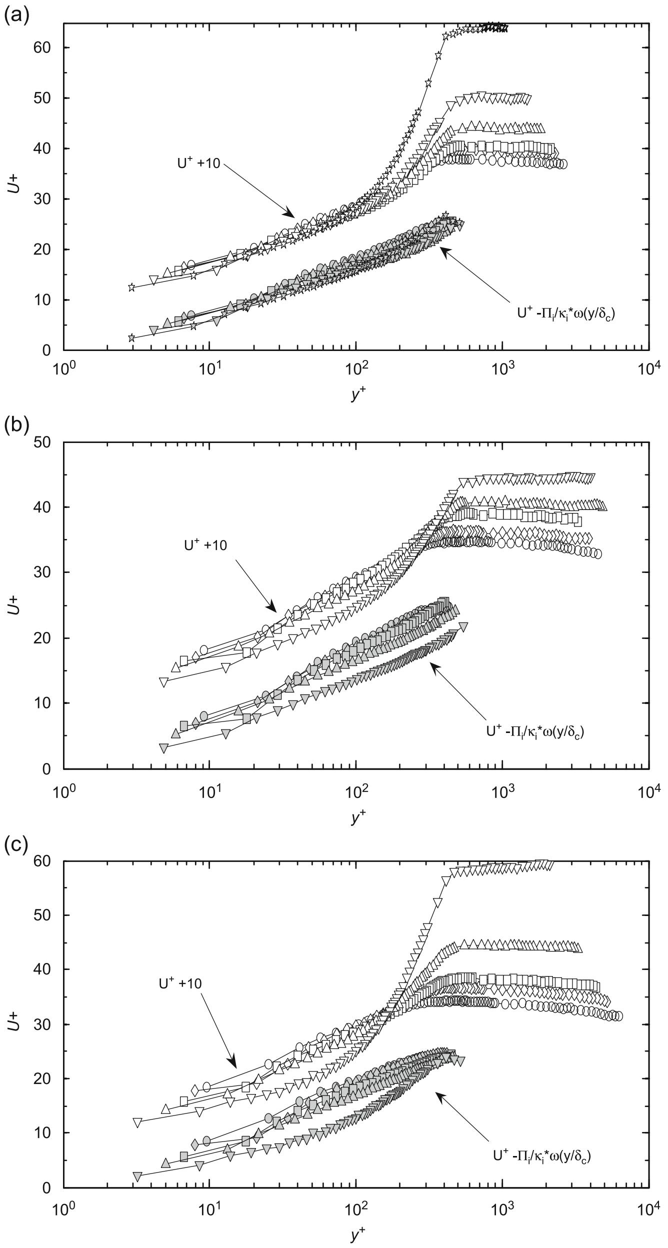

Fig. 4. Velocity profiles with inner coordinates (open symbols) and associated wake laws (solid grey symbols), $\alpha = 10^\circ$, $\mathrm{Re} = 5 \times 10^5$: (a) NACA0015, (b) NACA0025 and (c) NACA0035.

3.3. Hysteretic behaviour and fluctuating efforts

For the NACA0015 and NACA0025 profiles, an abrupt loss of lift, characteristic of stall, is observed for an incidence angle of 21° and 33°, respectively. For flow reattachment, the incidence angle must be drastically reduced to 15° and 23°, respectively. This behaviour is illustrated in Fig. 5 in which the hysteresis loops have been highlighted by arrows following the cycle of the lift coefficient. In fact, the cycle provides upper and lower branches characterised by two different states of the flow. The starting point for the flow along the increasing angle branch (upper branch) is a partially detached flow (called state I) in which the detachment point progressively moves from the trailing edge to the leading edge. On the decreasing angle branch (lower branch), a massively separated flow is observed (called state II).

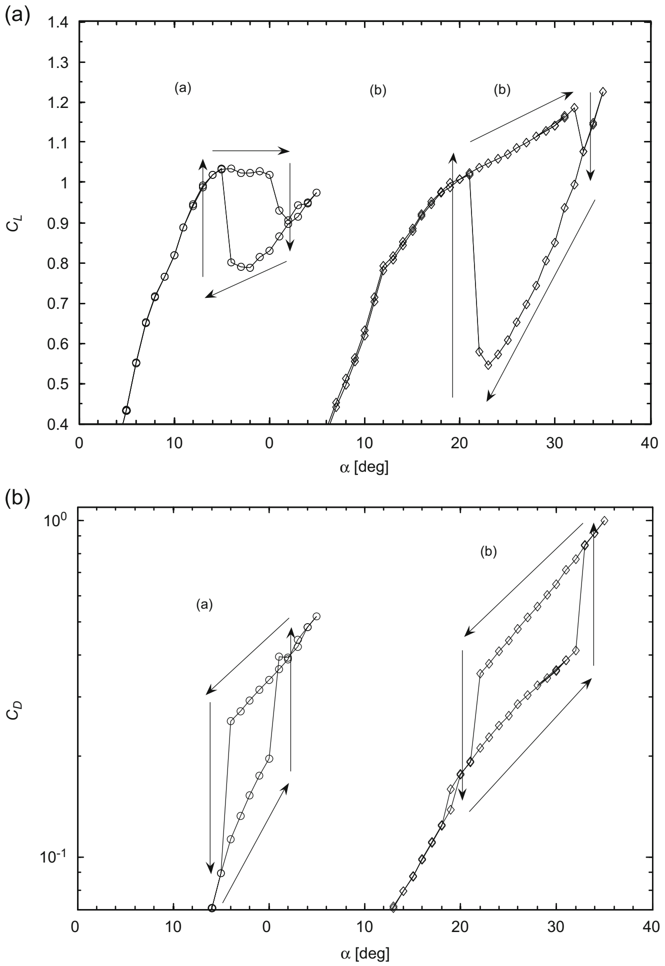

Fig. 5. (A) Close-up of the hysteretic behaviour of the lift coefficients, and (B) the drag coefficients, for (a) NACA0015 and (b) NACA0025.

The corresponding boundary layer pattern has been observed and described in detail in the section devoted to separated flow. This phenomenon is not observed on the thickest profile in the range of our investigation; we had to increase the incidence angle up to 40° to observe a similar phenomenon. The rms values of the lift and drag coefficients at the stall angle show that the hysteretic behaviour is associated with an abrupt increase in the fluctuation of forces as shown in Fig. 6. This increase in the fluctuating part is associated with the unsteady component of the hydrodynamic coefficients.

4. Unsteady separated flow

4.1. Strouhal number

The lift and drag fluctuations that have been described are related to the large scale structures of the flow, which will be characterised in the two different states. The ejection of the vortices was quantified by the LDV measurements in the wake of the three profiles for several angles of incidence. The related velocity spectra are shown in Fig. 7 against the incidence angles and frequencies. In the three figures, no predominant frequency is observed for an incidence lower than 20°. When incidence was raised over 20°, an organised motion due to the regular vortex shedding appeared. This shedding is characterised by a predominant frequency, *f*. The evolution of the von Kármán instability is shown in Fig. 7, and the establishment of the instability is associated with an increase in the maximum spectral amplitude and a decrease

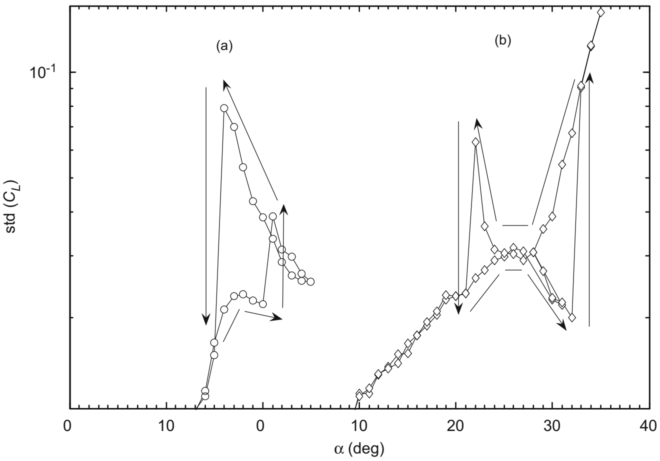

Fig. 6. Close-up of the hysteretic behaviour of the fluctuating effort lift for (a) NACA0015 and (b) NACA0025.

in the frequency. For NACA0015, the predominant frequency evolves linearly, but for the two thicker profiles, two different slopes can be observed if the behaviour remains linear. These different evolutions are characterised by two values of the Strouhal number, which is based on the projected area of the foil and defined as

$$\mathrm{St} = c \sin\alpha \frac{f}{U}. \tag{1}$$

This number reported versus the incidence angle for each profile is shown in Fig. 8. Two states of the flow are shown, which are characterised by two values of St (0.3 in state I and 0.2 in state II). The transition between the two states is characterised by a jump in the value of the Strouhal number.

A vortex shedding can be observed through the spectral analysis, and the shear layer at the separation point is affected by the Kelvin–Helmholtz instability. This instability, forced by the periodic vortex shedding, leads to an oscillation of the detachment point. The nonlinear interaction between these two instabilities appears to be responsible for the coexistence of states I and II (Hoarau and Braza, 2004).

4.2. Boundary layer state during hysteresis

On the NACA0015 hydrofoil, the boundary layer measurements were performed in the range of angle where the hysteretic behaviour was observed at the same incidence angle for both flow states. The incidence angles chosen were 16° and 20°. The same measurements were performed on the NACA0025 hydrofoil for the two specific states at $\alpha = 25°$. When the incidence angle of the foil was increased, two phenomena simultaneously occurred on the foil. The transition point and the detachment points moved towards the leading edge, and the distance between the two points decreased. Also, the detachment point behaved more and more erratically.

These phenomena can be observed in Fig. 9, which shows the velocity profiles of the two hydrofoils for the two flow states. For the thinner profile, the transition from states I to II is characterised by an abrupt modification in the location of the detachment point from $x/c = 0.45$ for state I to $x/c = 0.023$ for state II. On the NACA0025, the magnitude of the displacement of the detachment point is less pronounced ($x/c = 0.35$ for state I and $x/c = 0.043$ for state II). To conclude, for a low incidence angle, the thickness of the turbulent boundary layer increases with the thickness of the hydrofoil. At stall, the amplitude of the displacement of the detachment point decreases with an increase in the thickness of the profile; leading to a smaller decrease in the lift. This effect corroborates the well-known stall mechanism of the thick profile.

In Fig. 10, the local velocity on the suction side of the hydrofoil is presented against the x coordinate as a C_p value. It can be seen that for the two conditions that prevail just before stall, the maxima of the velocity (corresponding to minimum C_p) are equal for the two profiles. After stall (corresponding to state II), the thickness effect induces an increase in the velocity on the thicker profile. Thus, it seems that for a fixed Reynolds number, a velocity threshold (that cannot be overcome by the flow) exists.

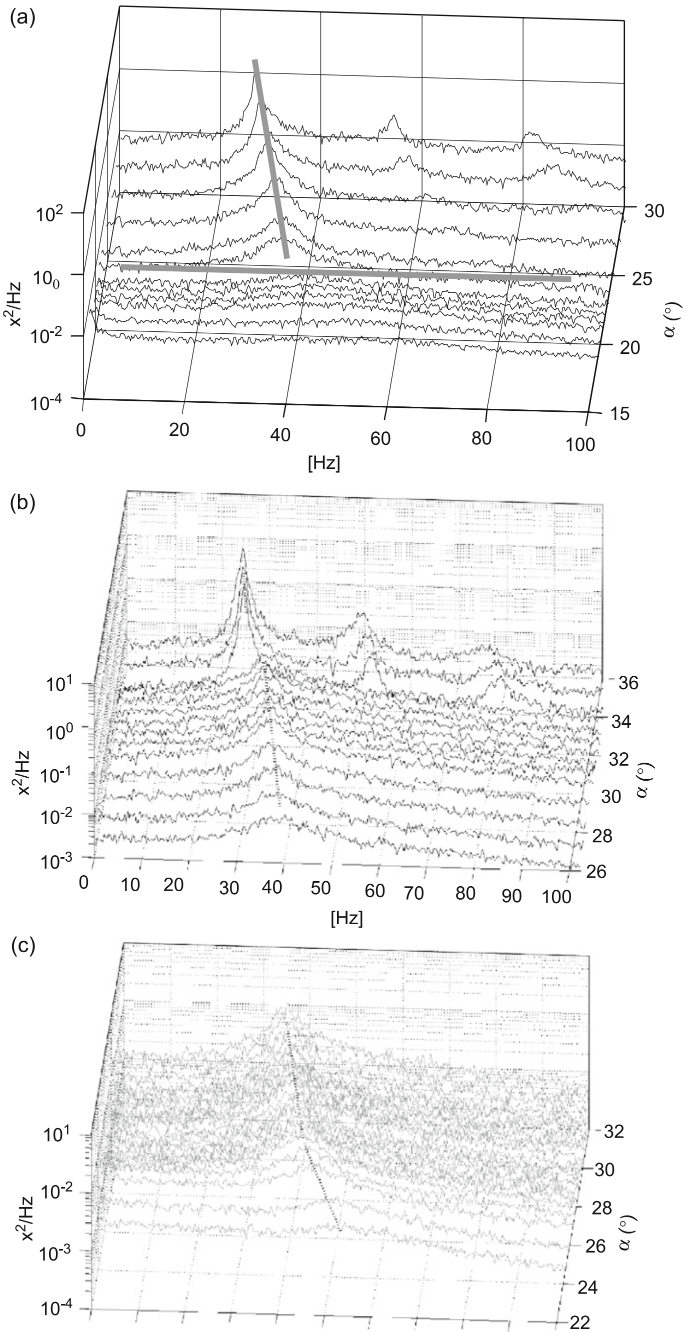

Fig. 7. Frequency spectra of the vertical velocity in the shear layer for the three profiles: (a) NACA0015 for $\alpha = 17$–$30°$, (b) NACA0025 for $\alpha = 26$–$35°$ and (c) NACA0035 for $\alpha = 22$–$31°$.

4.3. *Vortex dynamics during hysteresis*

At a high incidence angle, the near wake of the profile is characterised by the formation of organised motion. The value of the Strouhal number corresponds to the establishment of von Kármán alternating vortices depending on the position of the detachment point of the boundary layer. To better understand the jump in the Strouhal number at

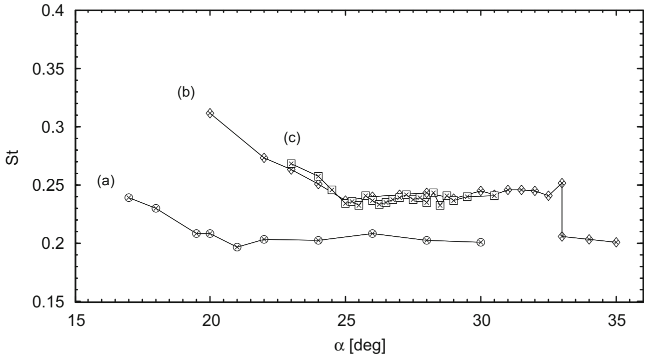

Fig. 8. Strouhal numbers versus incidence for the three profiles: (a) NACA0015, (b) NACA0025 and (c) NACA0035.

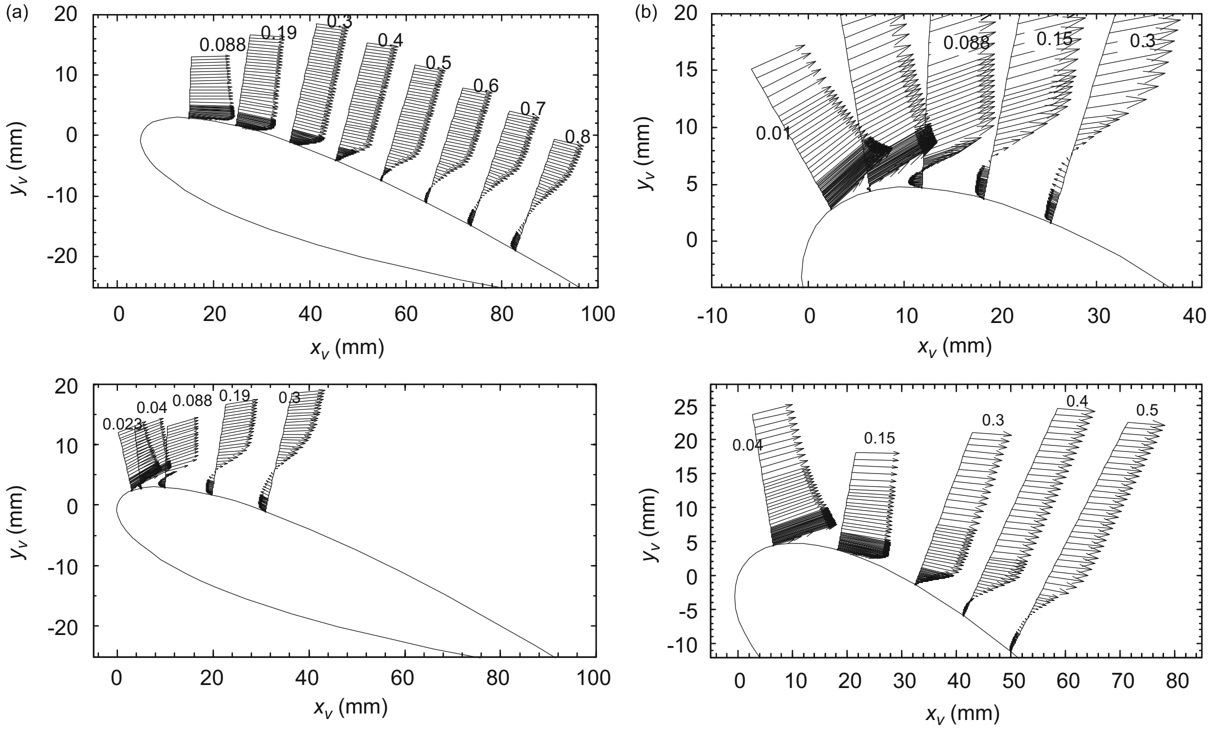

Fig. 9. (a) Velocity profiles for NACA0015 at 16° corresponding to State I (top), and State II (bottom). (b) Velocity profiles for NACA0025 at 25° corresponding to State I (top), and State II (bottom).

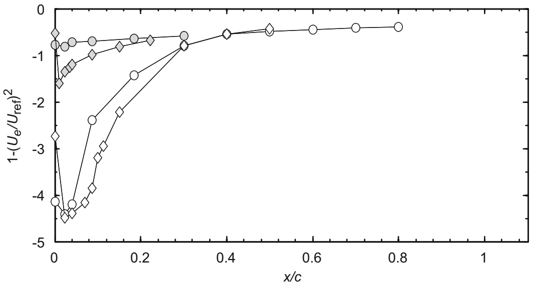

Fig. 10. Velocity on the two hydrofoil profiles (suction side) just before (open symbols) and just after (solid symbols) the occurrence of stall: ○, NACA0015, $\alpha = 16°$; ◇, NACA0025, $\alpha = 25°$.

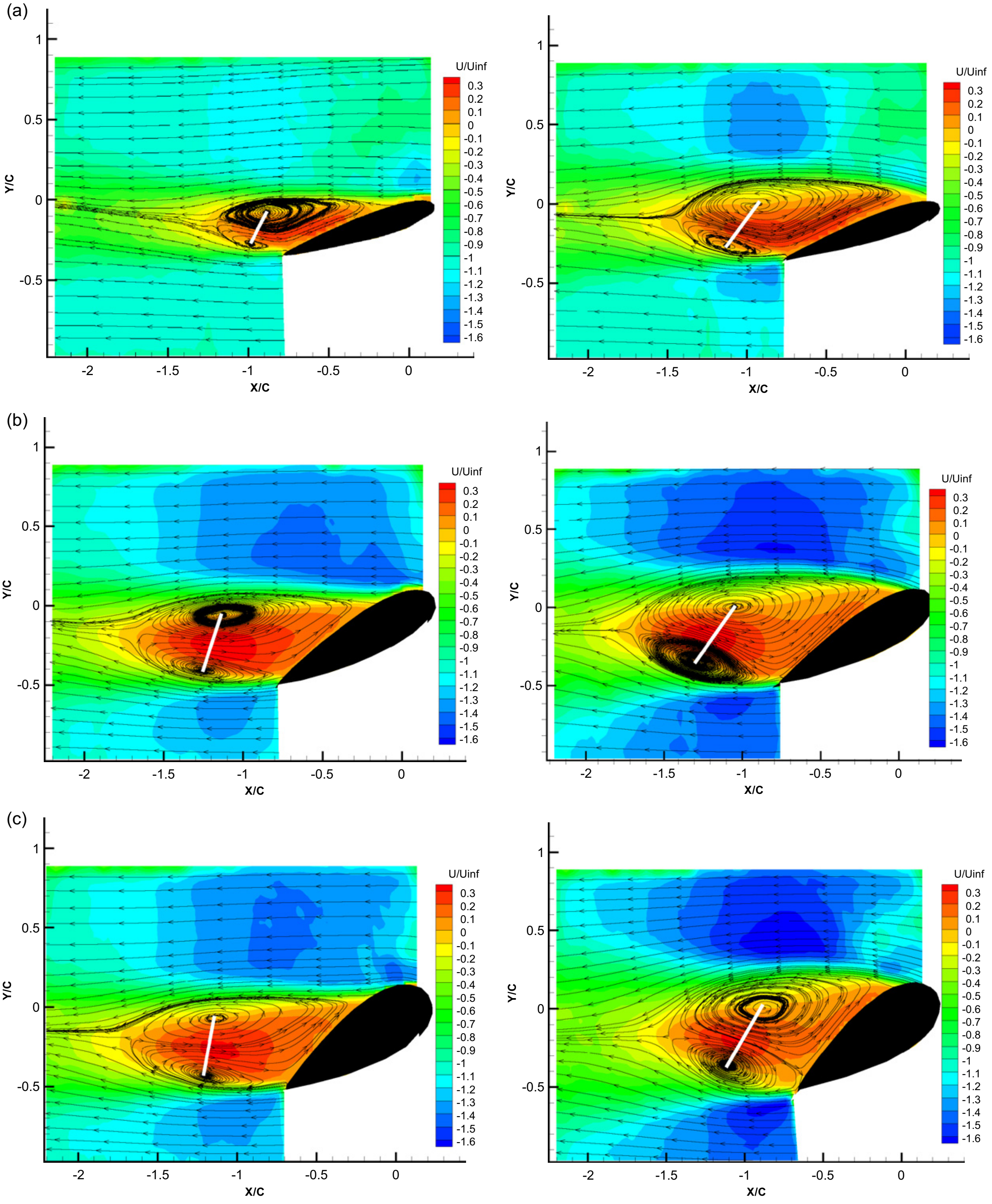

Fig. 11. Streamlines and iso-contours of mean longitudinal velocity *u*, at State I (left), State II (right) for the three hydrofoils: (a) NACA0015, (b) NACA0025 and (c) NACA0035.

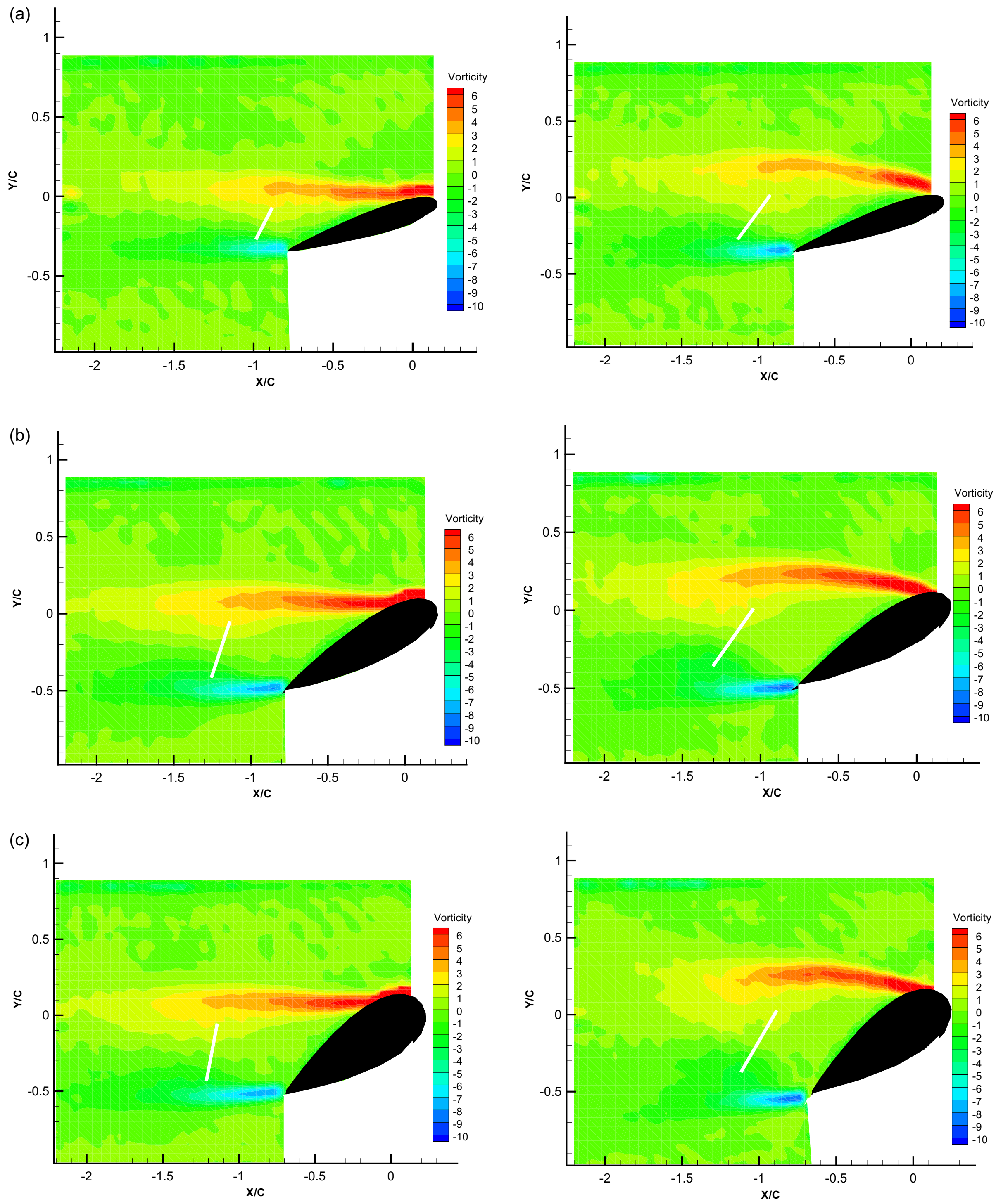

Fig. 12. Contours of iso-vorticity State I (left) and State II (right), for the three hydrofoils: (a) NACA0015, (b) NACA0025 and (c) NACA0035.

the passage from states I to II, cartography of the Reynolds averaged quantities are provided. In this section, emphasis is placed on the physical analysis of the mechanism governing the ejection of the leading and trailing edge vortices.

4.3.1. Topology of the coherent motion

The topology of the mean and turbulent flows is studied for the three hydrofoils at incidences corresponding to States I and II. The streamlines and iso-U contours, Fig. 11, and iso-vorticity contours, Fig. 12, are shown and compared during the hysteretic loop. As expected, a pattern of two symmetric eddies appears, which is due to averaging the passage of the alternating vortices from the leading and trailing edges (cyclonic and anticyclonic vortices, respectively). For a slight increase in the incidence angle, the specific streamlines for states I and II are presented; corresponding to the two-lobe structure. Saddle points can be observed in these figures, and the respective locations of the kernels of the vortices are highlighted in Fig. 11. The locations of the vortex core centres of the trailing and leading edge vortices and the saddle points in the wake are reported in Table 1 for the three hydrofoils and the two flow states.

The jump in the Strouhal number is associated with a relocation of the saddle point. The major change in the saddle point location can be seen for the thinner profile where the vertical movement is preponderant. For the cyclonic vortices (leading edge vortices), the movement of the vortex cores from State I to State II evidences a vertical transport of these vortices and a relative stability in the longitudinal direction. For the anticyclonic vortices (corresponding to the trailing edge vortices), the movement of the vortex cores from State I to State II shows a longitudinal transport of these vortices. The asymmetric transport corresponds to an angle variation of 51% between the two cores and the vertical direction. The establishment of vortex shedding at $\mathrm{St} = 0.2$ (corresponding to an increase in amplitude of the spectral density and a decrease in the dimensional frequency value) is globally associated with the vertical and longitudinal transport of the cyclonic and anticyclonic vortices, respectively. State II is characterised by an expansion of the wake in the downstream direction, which is associated with a thickening effect in the vertical direction as observed in the iso-U contours. The main difference between the two states is located near the separation, where the highest values of the vorticity are typically found, as shown in Fig. 12. The iso-contours of the vorticity show the formation of two shear layers: one from the leading edge and the other from the trailing edge. The classical formation length is greater from the leading edge than from the trailing edge for each profile at State I. Compared with the partially stalled hydrofoils (State I), the totally stalled case (State II) attenuates this previous difference. In summary, State I is characterised by an asymmetric vortex (elliptical and distorted vortex), and the trailing edge vortex is less developed than the leading edge vortex (anticyclonic vortices are strongly stretched). When entering State II, the anticyclonic vorticity region extends into a larger area. Furthermore, the growth of the average shear layer combined with roll up is completely developed downstream of the hydrofoils at State II in contrast with to State I. This behaviour is similar to that observed by Sicot et al. (2006) concerning the unsteady characteristics of the static stall of an airfoil at the same Reynolds number range.

On the other hand, small-scale disturbances grow in the core of the anticyclonic vorticity. Small-scale turbulent motions occur in the shear layer and the near wake just behind the profile for State II in contrast with State I, as shown in Fig. 13. The $\overline{u'^2}$ component has a two-lobe structure with a maximum value located near $x/c = -0.61$ and $y/c = \pm 0.25$ for the NACA0035 hydrofoil, in which the highest values are found near the detachment point. This small-scale agitation seems to enhance the horizontal diffusion of the trailing edge vortices and generates a stable vortex shedding as a von Kármán street. The extension of the maximum perturbation is located downstream of the recirculation area.

Table 1
Locations of the vortex cores and saddle points for the three profiles at States I and II.

		NACA0015		NACA0025		NACA0035	
		State I	State II	State I	State II	State I	State II
Vortex core centre (leading edge)	x/c	−0.884	−0.938	−1.125	−1.056	−1.139	−0.883
	y/c	−0.077	−0.002	−0.052	−0.005	−0.068	−0.009
Vortex core centre (leading edge)	x/c	−0.980	−0.129	−1.250	−1.297	−1.200	−1.115
	y/c	−0.275	−0.260	−0.404	−0.340	−0.431	−0.358
Saddle point	x/c	−1.193	−1.417	−1.662	−1.684	−1.660	−1.485
	y/c	−0.129	−0.089	−0.159	−0.162	−0.200	−0.171

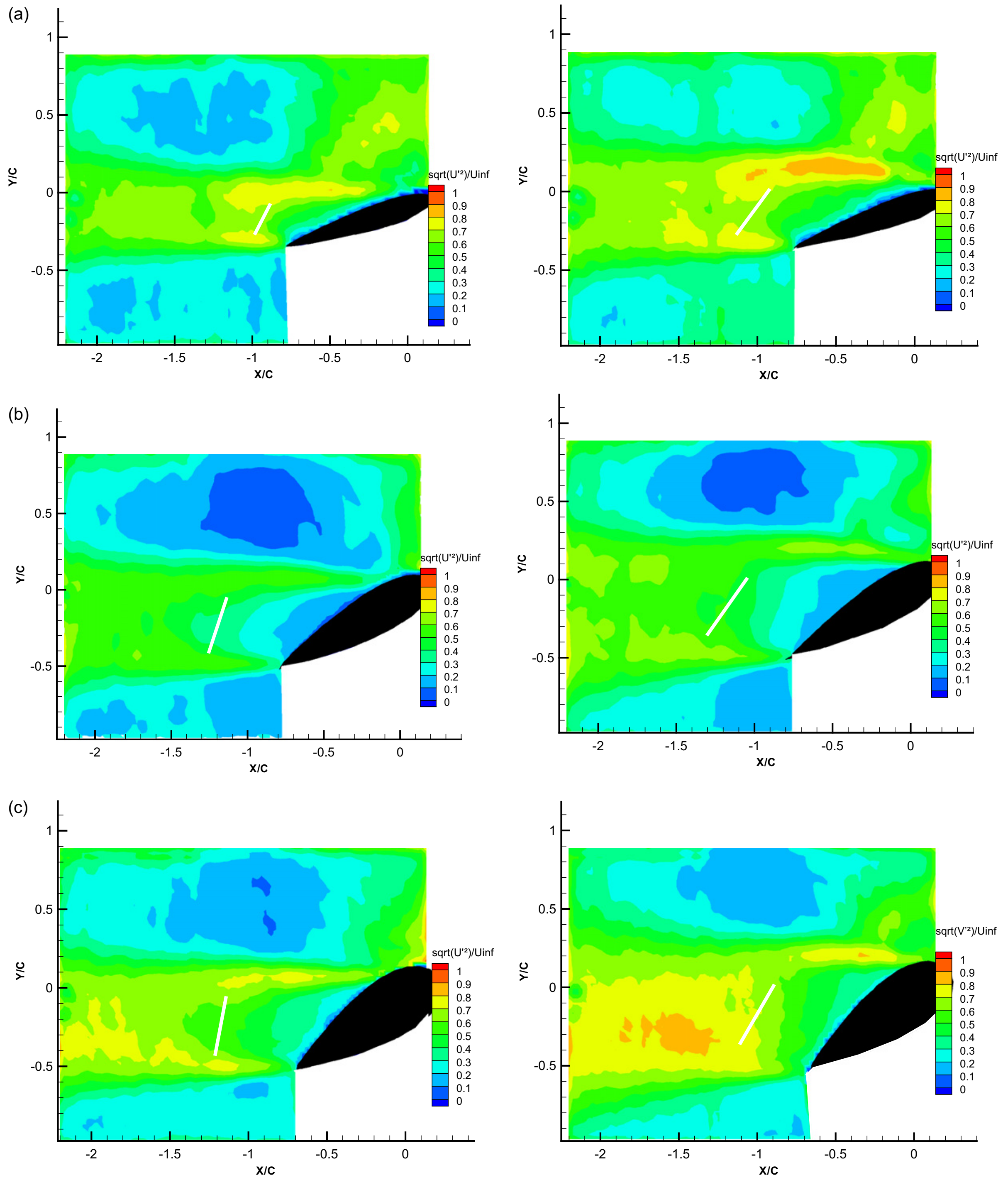

Fig. 13. Contours of iso-u'^2. State I (left) and State II (right), for the three hydrofoils: (a) NACA0015, (b) NACA0025 and (c) NACA0035.

Table 2
Characteristic length and aspect ratio of the wake behind the three profiles at State I and State II.

	NACA0015		NACA0025		NACA0035		Cylinder
	State I	State II	State I	State II	State I	State II	
l_c	3.86 ↗	4.35	3.43 ↘	3.37	3.05 ↘	2.59	1.37
l_u	2.80 ↘	2.65	1.20 ↗	1.55	1.28 ↗	1.35	0.81
e/l_c	0.340 ↘	0.335	0.382 ↗	0.420	0.414 ↗	0.542	0.828

4.3.2. Discussion of the physical aspect of vortex shedding

The streamlines and iso-U contours allow the determination of the recirculation length (l_c, given for the saddle point) and formation length (l_U, based on the location of the minimum axial velocity). To quantify the thickness effect on the vortex shedding process, a comparison with the classical case of the circular cylinder was proposed for an equivalent Reynolds number (Djeridi et al., 2003). To conserve the "wake similitude", characteristic lengths were normalised using the projected chord of the profile ($c \sin \alpha$). Additionally, the aspect ratio e/l_c, where e is the wake thickness based on the two-lobe structure, was determined. These values are reported in Table 2 for the three profiles.

It can be observed for State II that the three quantities approach the values for the cylinder, although this behaviour is more pronounced for the formation length and the aspect ratio for the two thicker profiles. The aspect ratios increased with the thickness of the hydrofoil and for the totally stalled case, except for the NACA0015. For this profile, the evolution of the characteristic length and the Strouhal number evolution versus incidence angle were different. The establishment of the von Kármán instability, associated with the modification of the wake pattern, was affected by the thickness effects and the amplitude of the vortex motions at State II. This behaviour must be linked with the lift fluctuations, and the maximum perturbation amplitude was observed for the NACA0015. For this profile, the separation point oscillation in the partially detached case is more pronounced; allowing the development of the Kelvin–Helmholtz instabilities at the leading edge, which govern the vortex shedding process and the roll up downstream of the hydrofoil.

Taking the previous results into account, it is necessary to propose a local definition of the vortices based on a non-intuitive concept. The vortex centres can be identified with the Q criterion as shown below:

$$Q = \tfrac{1}{2}(\|\Omega\|^2 - \|S\|^2), \tag{2}$$

where S is the rate-of-strain tensor and Ω the vorticity tensor (Jeong and Hussain, 1995). The calculated values correspond to the S_{12} and Ω_{12} values. According to this criterion, a vortex is a region in which the relative pressure is negative and $Q > 0$. The Q values are presented in Fig. 14 and compared for the two states of the flow for the three profiles. Additionally, a vortex can be defined as the location of the highest noise source and can be delimited by the two extrema of the spatial derivative of the divergence of the Lamb vector (Howe, 2002, 2004). The presence of the vorticity is responsible for the sound generation in a flow field, and this can be expressed using a combination of the Crocco equation of vorticity and the Lighthill aero-acoustic theory (Alim, 2007). To detect the location of the cyclonic and anticyclonic vortices in States I and II in the present study, we compared the divergence of the Lamb vector to define the vortex structure (as noisy structure) and the Q criterion. In Fig. 14, the major difference between States I and II is the location of the deformation area near the detachment point of the boundary layer and the larger diffusion of the positive value of Q downstream. The predominance of the strain rate in the wake is due to the turbulent agitation associated with the longitudinal transport of the trailing edge vortices and the vertical transport of the leading edge vortices. This turbulent agitation is accompanied by a diffusion of the divergence of the Lamb vector corresponding to the noisy structures in State II. Small-scale perturbations grew in the near core of the anticyclonic vortices as observed in Fig. 15, which shows the diagonal term of the tensor of the turbulence production, P_{12}, plotted with $Q = 0.5$. The maximum production was observed for the totally stalled case (State II) and was located downstream of the position of maximum vorticity. The predominant strain rate and the increase in turbulent production were located near the anticyclonic vortices corresponding to the realignment of the trailing edge vortices. Moreover, it can be seen that the turbulent production area is larger in State II than in State I for the leading edge vortices. This effect is due to the Kelvin–Helmholtz instabilities and the oscillations of the separation point.

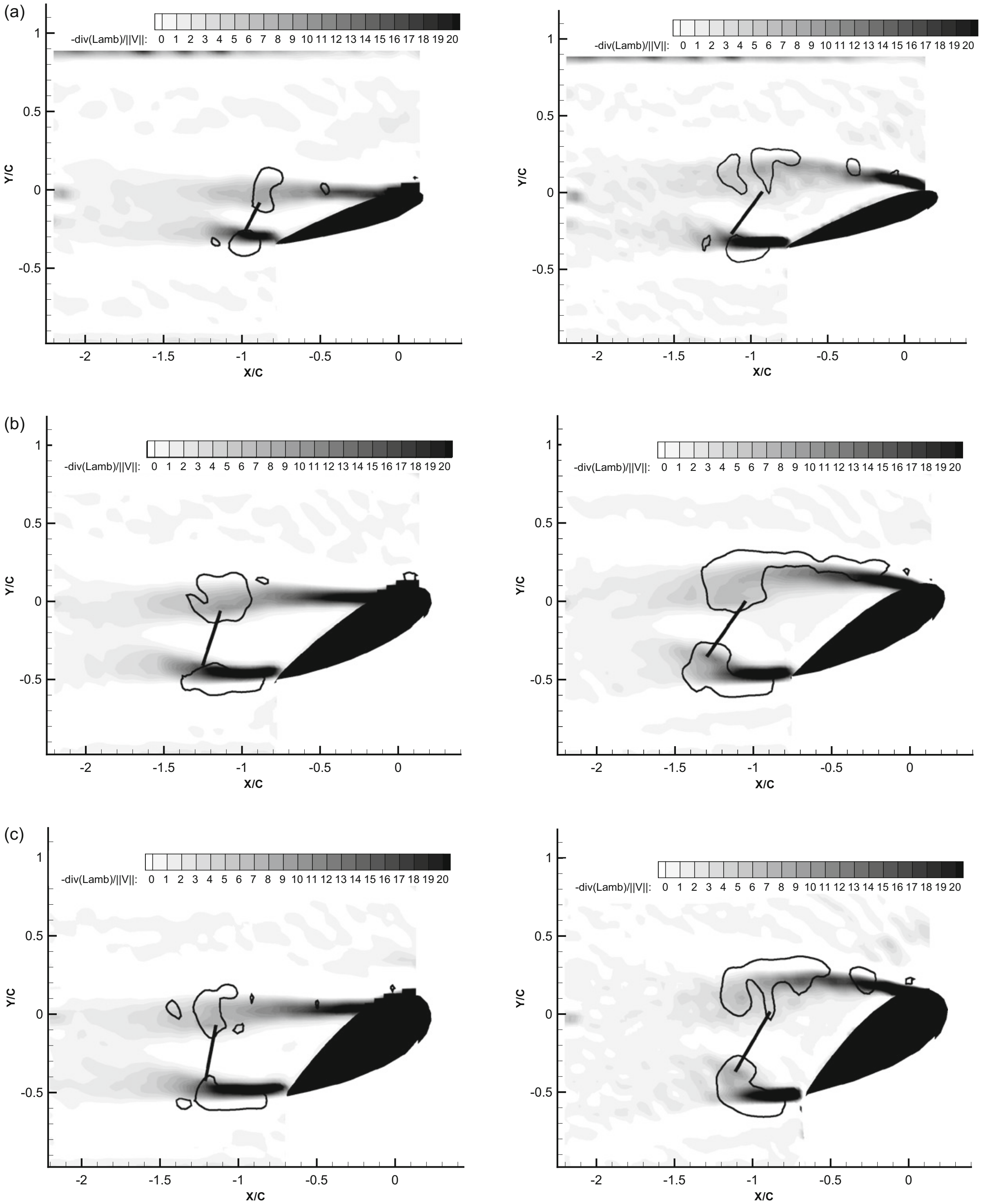

Fig. 14. *Q* and Lamb criteria for evaluation of the vortex centre position at State I (left) and State II (right), for the three hydrofoils: (a) NACA0015, (b) NACA0025 and (c) NACA0035.

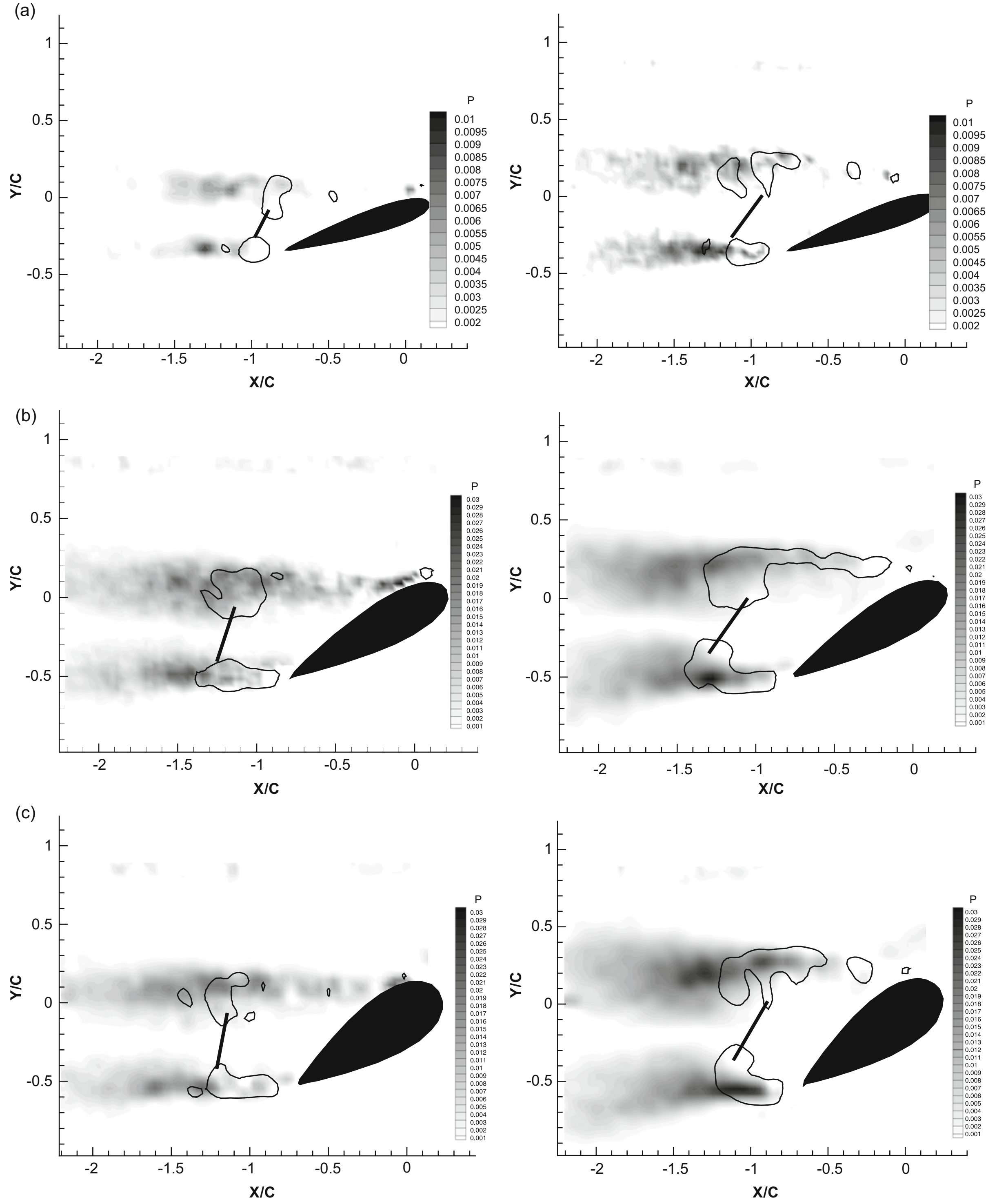

Fig. 15. Iso-contours of the turbulent production term, P_{12}, for the three profiles at State I (left) and State II (right), for the three hydrofoils: (a) NACA0015, (b) NACA0025 and (c) NACA0035.

5. Conclusions

This experimental work conducted on three symmetrical NACA profiles with relative thicknesses of 15%, 25% and 35% leads to the following conclusions.

Above roughly 10% thickness, the lift coefficient of the profile decreases when the thickness is increased. The hysteretic behaviour of the profile at stall is delayed when the thickness is increased, and this phenomenon is correlated with a modification of the flow state linked with the position of the detachment point, which is forced by the establishment of the von Kármán instabilities. For unsteady, separated flow at high incidence angle, the thickness effect is associated with a modification of the establishment of the von Kármán street. As observed through the spectral analysis for the thinner profile, the frequency evolved linearly, and the profiles of the two thicker hydrofoils exhibited different slopes if their behaviour remained linear.

The thickness of the profile tended to increase the thickness of the boundary layer at low incidence angle instead of at the stall condition, and the magnitude of the detachment point displacement was attenuated leading to a smaller decrease in the lift. The effect of the adverse pressure gradient required the use of two velocity laws to describe the entire velocity profile (near wall logarithmic law in the inner region and wake law in the outer region of the boundary layer). To account for the adverse pressure gradient, another law proposed by Coles was used to corroborate the hypothesis of a universal wake function. The thickness effect was then characterised by a deviation of the wake law accentuated for the two thicker profiles. For the hysteretic loop at static stall, the lower and upper branches corresponded to different flow states characterised by a severe modification of the vortex dynamics. The lower branch (State II) was characterised by a predominance of the strain rate in the wake due to the turbulent agitation associated with the longitudinal transport of the trailing edge vortices and the vertical transport of the leading edge vortices. This turbulent agitation was accompanied by a diffusion of the divergence of the Lamb vector corresponding to the noisy structures in State II and an increase in turbulent production.

To conclude, the thickness effects on the vortex shedding process induce:

(i) an increase of the oscillation amplitudes of the separation point;
(ii) a modification of the vortex roll up (mean diffusion and realignment);
(iii) the existence of "noisy" structures for the thicker profiles at totally stalled case (State II).

References

Alim, A., 2007. A physical comprehensive definition of a vortex based on the Lamb vector. Algerian Journal of Applied Fluid Mechanics 1 (1), 1–6.

Bourgoyne, D.A., Ceccio, S.L., Dowling, D.R., Jessup, S.D., Park, J.T., Brewer, W.H., Pankajakshan, R., 2000. Hydrofoil turbulent boundary layer separation at high Reynolds numbers. In: Twenty-third Symposium on Naval Hydrodynamics, Val de Reuil, France.

Bourgoyne, D.A., Hamel, J.M., Ceccio, S.L., Dowling, D.R., 2003. Time averaged flow over a hydrofoil at high Reynolds number. Journal of Fluid Mechanics 496, 365–405.

Bourgoyne, D.A., Ceccio, S.L., Dowling, D.R., 2005. Vortex shedding from a hydrofoil at high Reynolds number. Journal of Fluid Mechanics 531, 293–325.

Bradshaw, P., 1967. The turbulence structure of equilibrium boundary layers. Journal of Fluid Mechanics 29, 625–645.

Braza, M., Perrin, P., Hoarau, Y., 2006. Turbulence properties in the cylinder wake at high Reynolds numbers. Journal of Fluids and Structures 22 (6–7), 757–771.

Cantwell, B., Coles, D., 1983. An experimental study of entrainment and transport in the turbulent wake of a circular cylinder. Journal of Fluid Mechanics 136, 321–374.

Coles, D., 1956. The law of the wake. Journal of Fluid Mechanics 1, 191–226.

Cousteix, J., 1989. Aérodynamique – Turbulence et couche limite turbulente. Editions Cepadues.

Djeridi, H., Sarraf, C., Billard, J.Y., 2007. Thickness effect of the NACA symetric hydrofoils on the turbulent boundary layer pattern. In: IUTAM Symposium on Unsteady Separated Flows and Their Control, Kerkyra (Corfu), Greece, June 18–22.

Djeridi, H., Braza, M., Perrin, R., Harran, G., Cid, E., Cazin, S., 2003. Near wake turbulence around a circular cylinder at high Reynolds number. Journal of Flow, Turbulence and Combustion 71, 19–34.

Hoarau, Y., Braza, M., Ventikos, Y., Faghani, D., Tzabiras, G., 2003. Organized modes and the three-dimensional transition to turbulence in the incompressible flow around a NACA0012 wing. Journal of Fluid Mechanics 496, 63–72.

Hoarau, Y., Braza, M., 2004. Simulation et contrôle d'un écoulement fortement décollé autour d'un profil d'aile. 39ème colloque d'aérodynamique appliqué AAAF.

Howe, M.S., 2002. Theory of Vortex Sound. Cambridge University Press, Cambridge.

Howe, M.S., 2004. Mechanism of sound generation by low Mach number flow over a wall cavity. Journal of Sound and Vibration 273, 103–123.

Jeong, J., Hussain, F., 1995. On the identification of a vortex. Journal of Fluid Mechanics 285, 69–94.

Ludwieg, H., Tillman, W., 1950. Investigation of the wall-shearing stress in turbulent boundary layer. NACA Technical Memorandum No. 1285.

Lurie, E.A., Keenan, D.P., Kerwin, J.E., 1998. Experimental study of an unsteady separating boundary layer. AIAA Journal 36 (4), 565–570.

Marušic, I., Perry, A.E., 1995. A wall-wake model for the turbulence structure of boundary layers. Part 2. Further experimental support. Journal of Fluid Mechanics 298, 389–407.

Mellor, G.L., 1966. The effect of pressure gradients on turbulent flow near a smooth wall. Journal of Fluid Mechanics 24, 255–274.

Mellor, G.L., Gibson, D.M., 1966. Equilibrium turbulent boundary layers. Journal of Fluid Mechanics 24, 225–253.

Mittal, S., Saxena, P., 2000. Prediction of hysteresis associated with the static stall of an airfoil. AIAA Journal 38 (5), 933–935.

Mueller, T., 1985. The influence of laminar separation and transition on low Reynolds number airfoil hysteresis. Journal of Aircraft 22 (9), 763–770.

Na, Y., Moin, P., 1998. Direct numerical simulation of a separated turbulent boundary layer. Journal of Fluid Mechanics 374, 379–405.

Perrin, R., Braza, M., Cid, E., Cazin, S., Moradei, F., Barthet, G., Sevrain, A., Hoarau, Y., 2005. Near-wake turbulence properties in the high Reynolds incompressible flow around a circular cylinder by 2C and 3C PIV. In: Proceedings of the Sixth ERCOFTAC International Symposium on Engineering Turbulence Modelling and Measurements (ETMM6).

Perrin, R., Braza, M., Cid, E., Cazin, S., Chassaing, P., Mockett, C., Reimann, T., Thiele, F., 2008. Coherent and turbulent process analysis in the flow past a circular cylinder at high Reynolds number. Journal of Fluids and Structures 24 (8), 1313–1325.

Perry, A.E., Marušic, I., 1995. A wall-wake model for the turbulence structure of boundary layers. Part 1. Extension of the attached eddy hypothesis. Journal of Fluid Mechanics 298, 361–388.

Persillon, H., Braza, M., 1998. Physical analysis of the transition to turbulence in the wake of a cylinder by three-dimensional Navier–Stokes simulation. Journal of Fluid Mechanics 365, 23–88.

Sarraf, C., 2007. Etude expérimentale du comportement hydrodynamique de profils portants épais, étude de la couche limite. Ph.D. Thesis, Ecole Centrale de Nantes/Université de Nantes.

Sicot, C., Aubrun, S., Loyer, S., Devinant, P., 2006. Unsteady characteristics of the static stall of an airfoil subjected to freestream turbulence level up to 16%. Experiments in Fluids 41 (4), 641–648.

Thwaites, B., 1960. Incompressible Aerodynamics: An Account of the Theory and Observation of the Steady Flow of Incompressible Fluid Past Aerofoils, Wings and Other Bodies. Dover Publications.

Williamson, C.H.K., 1992. The natural and forced formation of spot-like vortex dislocations in the transition for a wake. Journal of Fluid Mechanics 243, 393–441.

Yang, Z., Voke, P.R., 2001. Large eddy simulation of boundary layer separation and transition at a change of surface curvature. Journal of Fluid Mechanics 439, 305–333.